# 9
# Resonance Raman Scattering: Experimental Observations of the Radial Breathing Mode

In the next three chapters, we present an in depth analysis of the resonance Raman scattering process, that makes possible the observation of the Raman spectra from isolated nanocarbons, such as a single-layer graphene [86], one isolated carbon nanotube [176] or an isolated nanoribbon [83]. Although resonance can occur in any nanocarbon material, in these chapters, we focus on the radial breathing mode (RBM) of nanotubes because the RBM is an especially instructive example of resonance Raman scattering. Because of the low frequency (low energy) of $\omega_{\mathrm{RBM}}$ and because of the one-dimensional character of carbon nanotubes, the RBM spectra are extremely informative about resonance Raman phenomena. Thus, the study of the RBM spectra can serve to give a clear picture on how Raman spectroscopy can be used to probe the electronic structure of nanotubes. Furthermore, the RBM-related science is so well developed that there are already sufficient experiments and theory in the literature to address most of the information one can generally extract from a Raman feature through its intensity ($I_{\mathrm{RBM}}$), frequency ($\omega_{\mathrm{RBM}}$), linewidth ($\Gamma_{\mathrm{RBM}}$), and the dependence of the three properties on the excitation laser energy ($E_{\mathrm{laser}}$), and also paying attention to environmental effects. Here the environmental effects refer to spectral changes associated with perturbations due to doping or arising from changes in the materials surrounding the SWNT. Since we are dealing with a nanomaterial, any surrounding material will play an important role in the observed optical-related properties, and the RBM spectra can also be used to probe such environmental conditions.

In this chapter, we start in Section 9.1 with the definition of the RBM and a description of its frequency dependence on the tube diameter, which can be simply derived from elasticity theory. In Section 9.2 we review the general optical properties of the RBM spectra in one isolated SWNT, including the resonance Raman effect, the resonance window, Stokes and anti-Stokes phenomena and polarization effects. The final Section 9.3 ends the chapter with an extension of the resonance Raman analysis discussed in Section 9.2 to SWNT samples with a broad $(n, m)$ distribution. These results will serve as a basis for the study of the carbon nanotube electronic structure, theoretically addressed in Chapter 10. Chapter 10 is very interesting from the physics point of view, by departing from the tight-binding description already introduced in Chapter 2, and by discussing the effect of $\sigma$–$\pi$ hybridization and of excitonic effects on the Raman spectra. Chapter 11 addresses

*Raman Spectroscopy in Graphene Related Systems*. Ado Jorio, Riichiro Saito, Gene Dresselhaus, and Mildred S. Dresselhaus

ISBN: 978-3-527-40811-5

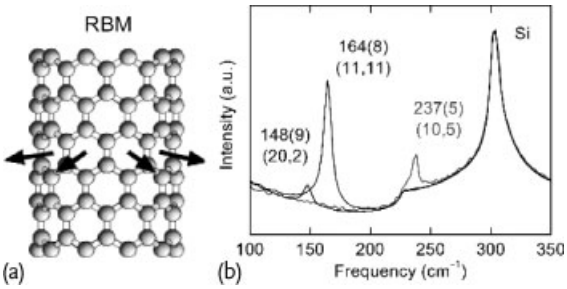


**Figure 9.1** (a) Schematic picture of the atomic displacements in the radial breathing mode (RBM). (b) Three superimposed Raman spectra of the RBM of three isolated SWNTs grown by the chemical vapor deposition (CVD) method and contained on a $Si/SiO_2$ substrate. The spectra are taken at three different spots on the substrate where the RBM Raman signal from resonant SWNTs are found. The RBM frequencies (linewidths) are displayed in $cm^{-1}$. Also shown are the $(n, m)$ indices assigned from the Raman spectra for each resonant tube. The step in the spectrum at $\sim$ 225 $cm^{-1}$ and the peak at 303 $cm^{-1}$, common to all spectra, come from the $Si/SiO_2$ substrate [176].

both the electron–photon and electron–phonon matrix elements and their effect on the observed Raman spectra.

## 9.1
## The Diameter and Chiral Angle Dependence of the RBM Frequency

As suggested by its name, in the radial breathing mode (RBM) all the C atoms are vibrating in the radial direction with the same phase, as if the tube were breathing (see Figure 9.1a). The atomic motion does not break the tube symmetry, that is, the RBM is a totally symmetric ($A_1$) mode. Since this particular vibrational mode only occurs in carbon nanotubes, it is used to distinguish carbon-based samples containing carbon nanotubes from $sp^2$ carbon samples that do not contain carbon nanotubes, and to give particular emphasis to samples containing single-wall carbon nanotubes (SWNTs), where the intensity of the RBM is strong compared with other nonresonant spectra coming from the substrate or with other resonance Raman spectra (see Figure 9.1b) [176]. A very important characteristic is the RBM frequency dependence on tube diameter ($\omega_{\mathrm{RBM}} \propto 1/d_t$). Although this dependence was first predicted using force constant calculations [278], an analytical derivation can be made using elasticity theory, that is the subject of Section 9.1.1. Later in Section 9.1.5 shows the small deviations from the simple inverse diameter dependence due to curvature effects and the Kohn anomaly.

### 9.1.1
### Diameter Dependence: Elasticity Theory

Here we show the dependence of the RBM frequency on the SWNT diameter. Elasticity theory describes the energetics of a continuous, homogeneous medium

under strain, and follows mostly from Hooke's law (strain being proportional to stress) and Newton's second law. Then the potential energy in an elastic medium is given by [95]:

$$U = \frac{1}{2}\sum_{\lambda=1}^{6}\sum_{\mu=1}^{6} C_{\lambda\mu}\, e_\lambda\, e_\mu \ , \tag{9.1}$$

where $C_{\lambda\mu}$ is the stiffness constant which relates strain and stress, and $e_\lambda$ (or $e_\mu$) is the strain. The sum in Eq. (9.1) is over all possible strain/stress axes ($\lambda, \mu = xx,\ yy,\ zz,\ yz,\ zx,\ xy$). Equation (9.1) is a general expansion from a harmonic potential $U = \frac{1}{2}Kx^2$. If we consider a uniaxial strain along $z$, it is common to use the Young's modulus ($Y = C_{zzzz}$), which is defined as the coefficient relating strain/stress to tension/deformation along $zz$.

The elastic energetics for the RBM can then be described by a one-dimensional-like tension/deformation. The variation in nanotube radius ($\delta R$) can be related to a one-dimensional strain $e$ along the radial direction $r$, which stretches the graphene sheet in the circumferential direction, associated with the nanotube by

$$e = \frac{\delta R}{R} \ , \tag{9.2}$$

and the related elastic energy will be given by

$$U = \frac{1}{2}\int Ye^2\, dV = \frac{1}{2}YV\left(\frac{\delta R}{R}\right)^2 \ , \tag{9.3}$$

from where, by considering a general vibration with a spring constant $k\,\omega = \sqrt{k/M}$, where $k$ is given by $YV/R^2$, we get

$$\omega_{\mathrm{RBM}} = \sqrt{\frac{YV}{MR^2}} = \sqrt{\frac{Y}{\rho}}\frac{1}{R} = \frac{A}{d_t} \ , \tag{9.4}$$

where $V$ is the volume and $M$ is the mass of the cylinder, $\rho = M/V$ is the density and $d_t$ is the tube diameter. The proportionality constant $A$ in Eq. (9.3) can be estimated from the elastic properties of graphite. By describing sound waves in terms of elasticity theory, we see that $\sqrt{Y/\rho}$ is the sound velocity for the longitudinal acoustic mode ($v_L = 21.4\,\mathrm{km/s}$) [279]. Therefore, $A$ describes the elastic behavior of an isolated SWNT in the large diameter limit, where elasticity theory is expected to be valid, thereby giving $A = 227\,\mathrm{cm^{-1}\,nm}$ [95, 259, 279, 280].

Figure 9.2 shows a plot of $\omega_{\mathrm{RBM}}$ vs. $d_t$ for 197 different SWNTs (of which 73 are metallic and 124 semiconducting) [31, 189]. For all the 197 SWNTs, their $(n, m)$ indices were assigned by experiment (extracted from Figure 9.15, discussed in Section 9.3.2) and their diameters were determined by the relation for tube diameter $d_t = a_{C\text{–}C}\sqrt{3(n^2 + mn + m^2)}/\pi$, where $a_{C\text{–}C} = 0.142\,\mathrm{nm}$ is the carbon–carbon distance (see Section 2.3.1). By thus fitting the experimental data shown in Figure 9.2 using the relation $\omega_{\mathrm{RBM}} = \boldsymbol{A}/d_t + \boldsymbol{B}$, we obtain $\boldsymbol{A} = (227.0 \pm 0.3)\,\mathrm{nm\,cm^{-1}}$ and $\boldsymbol{B} = (0.3 \pm 0.2)\,\mathrm{cm^{-1}}$. This result is in remarkably good agreement with elasticity theory, thus directly connecting one-dimensional carbon nanotubes and their

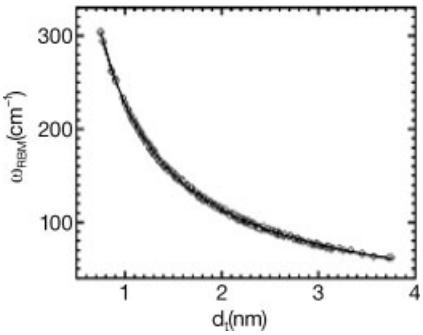


**Figure 9.2** Experimental radial breathing mode frequency ($\omega_{\mathrm{RBM}}$) as a function of tube diameter ($d_t$). Open circles represent experimental values and the solid line is given by $\omega_{\mathrm{RBM}} = 227.0/d_t + 0.3$ [189].

two-dimensional counterpart graphene from which nanotubes are conceptually derived.

Although experiment and elasticity theory agree perfectly in the experiment analyzed in Figure 9.2, these results have only been obtained, so far, for one specific type of SWNT, that is, SWNTs which are ultra-long, vertically aligned and grown by the water-assisted chemical vapor deposition (CVD) method [281]. Most of the RBM experimental results in the literature have been fitted with the relation $\omega_{\mathrm{RBM}} = \boldsymbol{A}/d_t + \boldsymbol{B}$, with values for the parameters $\boldsymbol{A}$ and $\boldsymbol{B}$ varying widely from paper to paper [189, 282], as discussed in the next section.

### 9.1.2 Environmental Effects on the RBM Frequency

As discussed in the previous section, the RBM resonance Raman scattering (RRS) of SWNTs grown by the water-assisted CVD method [281] follows the simplest linear relation between $\omega_{\mathrm{RBM}}$ and $d_t$, namely $\omega_{\mathrm{RBM}} = A/d_t$, with the proportionality constant $\boldsymbol{A} = 227.0\,\mathrm{cm}^{-1}\,\mathrm{nm}$, in agreement with the elastic properties of graphene [279], and with a negligible environmental effect ($\boldsymbol{B} \approx 0$) [189]. However, all the other experimental results in the carbon nanotube literature have been fitted with the relation $\omega_{\mathrm{RBM}} = \boldsymbol{A}/d_t + \boldsymbol{B}$, with values for $\boldsymbol{A}$ and $\boldsymbol{B}$ varying from one research group to another [172, 176, 180, 183, 184, 283–288]. A nonzero value for the empirical constant factor $\boldsymbol{B}$ prevents the expected limit of a graphene sheet from being achieved, where $\omega_{\mathrm{RBM}}$ should go to zero when $d_t$ approaches infinity. Therefore, $\boldsymbol{B}$ is supposedly associated with an environmental effect on $\omega_{\mathrm{RBM}}$, rather than an intrinsic property of SWNTs. The "environmental effect" here means the effect of the surrounding medium, such as bundling, molecules adsorbed from the air, the surfactant used for the SWNT bundle dispersion, the substrates on which the tubes are sitting, etc. As we will discuss here, all the observed $\omega_{\mathrm{RBM}}$ values reported in the literature are upshifted from the fundamental relation ($\omega_{\mathrm{RBM}} = 227/d_t$, with $B = 0$), the upshift exhibiting a $d_t$ dependence in quantitative agreement with

recent predictions which consider the van der Waals interaction between SWNTs and their environment [189].

In Figure 9.3 we compare similar $\omega_{\mathrm{RBM}}$ Raman spectra taken from two different samples. The gray lines show the $\omega_{\mathrm{RBM}}$ spectra for the "super-growth" SWNTs which are compared to the black line $\omega_{\mathrm{RBM}}$ spectra obtained from a SWNT sample grown by the alcohol-assisted CVD method [287]. Comparing the spectra in Figure 9.3a and b it is clear that the $\omega_{\mathrm{RBM}}$ values for the "alcohol-assisted CVD" sample are upshifted from the "super-growth" $\omega_{\mathrm{RBM}}$ frequencies.[1)]

Figure 9.4a shows the difference between several determinations of $\omega_{\mathrm{RBM}} = \boldsymbol{A}/d_{\mathrm{t}} + \boldsymbol{B}$ found in the literature [172, 176, 180, 183, 184, 286, 287] and the $\omega_{\mathrm{RBM}} = 227.0/d_{\mathrm{t}}$ relation for the "super-growth" samples. All the curves in the literature converge within the 1 to 2 nm $d_{\mathrm{t}}$ range, which is the diameter range for which most of the experimental data were actually obtained. Figure 9.4b shows the difference between the actual experimental values for $\omega_{\mathrm{RBM}}$ from the literature ($\omega_{\mathrm{RBM}}^{\mathrm{Lit.}}$) [176, 183, 184, 283–288] and for the "super-growth" (S.G) sample ($\omega_{\mathrm{RBM}}^{\mathrm{S.G.}}$), as a function of $d_{\mathrm{t}}$. All the published results for $\omega_{\mathrm{RBM}}^{\mathrm{Lit.}}$ are grouped in Figure 9.4b on a $d_{\mathrm{t}}$-dependent upshifted trend for $\Delta\omega_{\mathrm{RBM}} = \omega_{\mathrm{RBM}}^{\mathrm{Lit.}} - \omega_{\mathrm{RBM}}^{\mathrm{S.G.}}$. Therefore, the $d_{\mathrm{t}}$ dependence of the difference between the experimental data in the literature and the fundamental relation $\omega_{\mathrm{RBM}} = 227.0/d_{\mathrm{t}}$ is always of the same sign, as shown in Figure 9.4b.

The problem of addressing the environmental effect on $\omega_{\mathrm{RBM}}$ is now reduced to solving a simple harmonic oscillator equation for a cylindrical shell subjected to an inwards pressure ($p(x)$) given by [189, 279]:

$$\frac{2x(t)}{d_{\mathrm{t}}} + \frac{\rho}{Y}(1-\nu^2)\frac{\partial^2 x(t)}{\partial t^2} = -\frac{(1-\nu^2)}{Yh}p(x)\,, \tag{9.5}$$

where $x(t)$ is the displacement of the nanotube in the radial direction, $p(x) = (24\,K/s_0^2)x(t)$, and K (in eV/Å$^2$) gives the van der Waals interaction strength, $s_0$ is

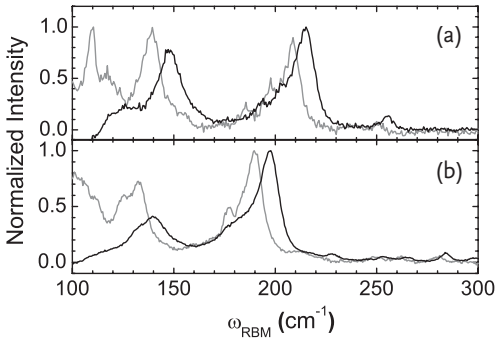


**Figure 9.3** The $\omega_{\mathrm{RBM}}$ spectra for "super-growth" SWNTs (gray) and for "alcohol CVD" SWNTs (black). The spectra are obtained using different laser lines: (a) 590 nm (gray) and 600 nm (black); (b) 636 nm (gray) and 650 nm (black) [189].

1) The differences in the low frequency region (below $\sim 120\,\mathrm{cm}^{-1}$) are due to different $d_{\mathrm{t}}$ distributions among various nanotube samples.

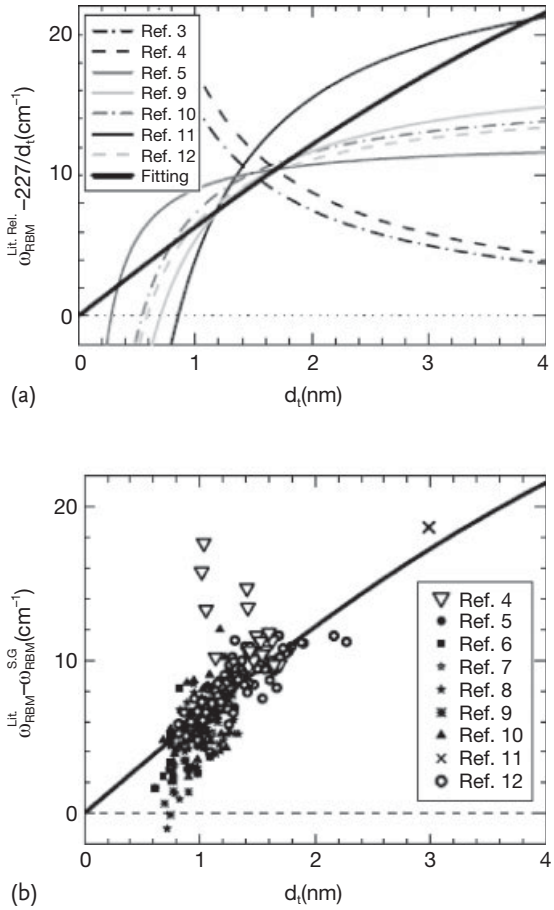


**Figure 9.4** (a) Difference between the $\omega_{\mathrm{RBM}}$ dependence on $d_t$ from the literature ($\omega_{\mathrm{RBM}}^{\mathrm{Lit.\ Rel.}}$) values and the $\omega_{\mathrm{RBM}} = 227.0/d_t$ relation as a function of tube diameter $d_t$. (b) Difference between the experimental $\omega_{\mathrm{RBM}}$ data from the literature ($\omega_{\mathrm{RBM}}^{\mathrm{Lit.}}$) and the $\omega_{\mathrm{RBM}}$ data for the "super-growth" sample ($\omega_{\mathrm{RBM}}^{\mathrm{S.G.}}$) as a function of $d_t$ [189]. Each symbol in (b) represents data from a different reference (see [189] for the references in the legends to (a) and (b) of this figure). The thick solid line is a fit to the data in (b), as discussed in the text, and also shown in (a) [189].

the equilibrium separation between the SWNT wall and the environmental shell, $Y$ is the Young's modulus ($69.74 \times 10^{11}$ g/cm s$^2$), $\rho$ is the mass density per unit volume (2.31 gm/cm$^3$), $\nu = 0.5849$ is Poisson's ratio and $h$ represents the thickness of the shell [279]. If $p(x)$ vanishes, Eq. (9.5) gives the fundamental frequency $\omega_{\mathrm{RBM}}^0$ for a pristine SWNT in units of cm$^{-1}$,

$$\omega_{\mathrm{RBM}}^0 = \left\{ \frac{1}{\pi c} \left[ \frac{Y}{\rho(1-\nu^2)} \right]^{1/2} \right\} \frac{1}{d_t} \,, \tag{9.6}$$

where the term inside the curly bracket in Eq. (9.6) gives the fundamental value of $A = 227.0\,\mathrm{cm}^{-1}\,\mathrm{nm}$.[2] For a nonvanishing $p(x)$ we have

$$\omega'_{\mathrm{RBM}} = 227.0\left[\frac{1}{d_t^2} + \frac{6(1-\nu^2)}{Yh}\frac{K}{s_0^2}\right]^{1/2}, \tag{9.7}$$

where $[6(1-\nu^2)/Yh] = 26.3\,\text{Å}^2/\mathrm{eV}$. The shift in $\omega'_{\mathrm{RBM}}$ due to the environment is given by $\Delta\omega_{\mathrm{RBM}} = \omega'_{\mathrm{RBM}} - \omega^0_{\mathrm{RBM}}$. The data in Figure 9.4b is fitted (see thick black solid line) by considering $K/s_0^2$ in Eq. (9.7) as an adjustable parameter. The best fit is obtained with $K/s_0^2 = (2.2 \pm 0.1)\,\mathrm{meV/Å}^4$. The $d_t$-dependent behavior of the environmental effect in $\omega_{\mathrm{RBM}}$ is then established in Figure 9.4 for $d_t$ up to $d_t = 3\,\mathrm{nm}$. A similar environmental effect is obtained for SWNTs in bundles [172, 287], surrounded by different surfactants [180, 183, 184, 283–285], suspended in air by posts [286], or sitting on a $SiO_2$ substrate [176], but this environmental effect is absent in "super-growth" SWNTs.

For simplicity, all the $\omega_{\mathrm{RBM}}$ results in the literature which are upshifted from the pristine values due to the van der Waals interaction with the environment can be generally described by:

$$\omega^{\mathrm{Lit.}}_{\mathrm{RBM}} = \frac{227}{d_t}\sqrt{1 + C_e * d_t^2}\,, \tag{9.8}$$

where $C_e = [6(1-\nu^2)/Eh][K/s_0^2]\,(\mathrm{nm}^{-2})$ gives the effect of the environment on $\omega_{\mathrm{RBM}}$. Table 9.1 gives the the $C_e$ values fitting the RBM results for several samples in the literature. For $d_t < 1.2\,\mathrm{nm}$, where the curvature effects become important, the environmental effect depends more critically on the specific sample (i. e., $C_e$ for one SWNT sample on $SiO_2$ may differ from another sample on $SiO_2$ in the literature), and the observed environmental-induced upshifts range from 1 to $10\,\mathrm{cm}^{-1}$ for small diameter tubes within bundles or wrapped by different surfactants (e. g., SDS (sodium dodecyl sulfate) or single-stranded DNA). This effect gets even stronger when considering the effect of the outer tube on the inner tube in a double-wall carbon nanotube (DWNT), as discussed in the next section.

**Table 9.1** Strength of the environmental effect on the RBM frequency as measured by the $C_e$ factor in Eq. (9.8) which fits different SWNT samples in the literature.

| $C_e$ | Sample | Reference |
|---|---|---|
| 0 | Water-assisted CVD | Araujo [189] |
| 0.05 | HiPCO@SDS | Bachilo [288] |
| 0.059 | Alcohol-assisted CVD | Araujo [287] |
| 0.065 | SWNT@$SiO_2$ | Jorio [176] |
| 0.067 | Free-standing | Pailet [286] |

2) Equation (9.6) is different from Eq. (9.3) because in Eq. (9.6) we consider the Poisson ratio $\nu \neq 0$, and the $(1/2\pi c)$ term used to measure frequency in $\mathrm{cm}^{-1}$ is given explicitly.

### 9.1.3
### Frequency Shifts in Double-Wall Carbon Nanotubes

The inner and the outer tubes of a DWNT can be either metallic (M) or semiconducting (S).[3] Thus, the following four configurations are possible: M@M, M@S, S@S, and S@M, where S@M denotes an S inner tube inside an M outer tube, following the common notation for fullerenes [289, 290]. Each DWNT configuration is expected to possess distinct electronic properties. In particular, for the S@M configuration, the S inner tube of a DWNT could be regarded as a good approximation for an isolated semiconducting SWNT that is electrostatically shielded and physically protected from the local environment by an outer metallic tube. Therefore, the experimental data from the inner tubes can be used as a standard when compared to SWNTs that are subjected to environmental effects, such as contact with a substrate, water, oxygen, or charged molecular species [290].

Most spectroscopic experiments on DWNTs have been performed on bundles or solution-based samples [291–296], so that it has been inherently difficult to use Raman spectra to investigate which inner $(n, m)$ tubes are actually contained inside the variety of observed outer $(n', m')$ tubes (see Figure 9.5a). In order to quantitatively determine which specific inner and outer tubes actually form each DWNT, one must perform Raman experiments on individual DWNTs (see Figure 9.5c). Techniques that combine the use of E-beam lithography, atomic force microscopy (AFM) and Raman mapping have been developed to measure the Raman spectra from the inner and outer layers of the same individual DWNTs (see Figure 9.5) [289, 290].

An investigation of the Raman spectra of 11 isolated $C_{60}$-DWNTs, all with (6,5) semiconducting inner tubes and all with the S@M configuration was performed using a single laser excitation energy of $E_{\text{laser}} = 2.10\,\text{eV}$ [290]. The outer tubes of the 11 DWNTs that are formed with a (6,5) inner tube can have different $(n, m)$ designations from one another but some outer tubes will have common $(n, m)$ chiralities. The radial breathing mode (RBM) frequencies $\omega_{\text{RBM,o}}$ for the outer tube for such a DWNT as a function of $\omega_{\text{RBM,i}}$ for the inner tube are shown in Figure 9.6a. In this figure we see that for these 11 individual isolated DWNTs, $\omega_{\text{RBM,o}}$ for the outer tubes varies over a $12\,\text{cm}^{-1}$ range, while $\omega_{\text{RBM,i}}$ for the inner tubes (which all correspond to (6,5) tubes) does not have a constant value, but rather varies over a range of $18\,\text{cm}^{-1}$. This $18\,\text{cm}^{-1}$ variation in the RBM frequency $\omega_{\text{RBM,i}}$ for the inner tube is large, considering that all these inner tubes are (6,5) tubes. These experiments tell us that in forming a DWNT, the inner and outer tubes impose considerable stress on one another. This is suggested by the fact that the nominal wall to wall distances $\Delta d_{\text{t,io}}$ between the inner (i) and outer (o) tubes of the DWNTs are less than the $c$-axis distance in graphite (0.335 nm). In fact Figure 9.6b shows that $\Delta d_{\text{t,io}}$ values as small as 0.29 nm can be observed, implying a decrease of up

3) In discussing DWNTs, there are two methods for preparing DWNTs, one from heat-treating $C_{60}$ containing SWNTs (called peapods) and denoted by $C_{60}$-DWNTs, and a second CVD-based method denoted by CVD-DWNTs. Since the two methods lead to DWNTs with different diameter distributions they have somewhat different characteristics.

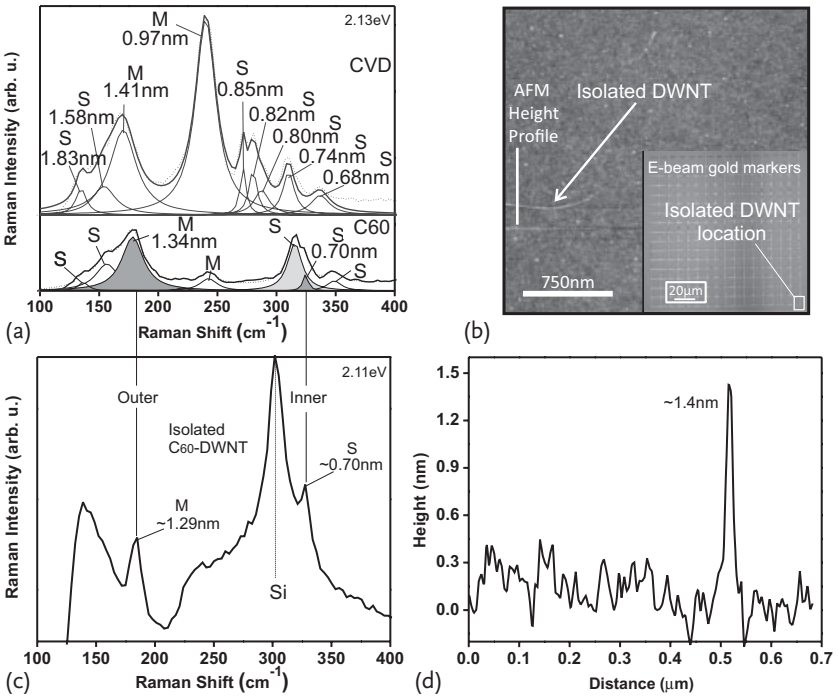


**Figure 9.5** (a) Raman spectra for the RBM region for CVD-DWNT and $C_{60}$-DWNT bundles ($E_{laser}$ = 2.13 eV). (b) Atomic force microscope (AFM) image of one individual, isolated DWNT. Inset: Silicon substrate with Au markers showing the location of the DWNT. (c) Raman spectra for the RBM Raman region ($E_{laser}$ = 2.11 eV) for an isolated individual $C_{60}$-DWNT and (d) AFM height profile of the individual, isolated DWNT shown in (b) with the RBM spectrum shown in (c). The vertical lines connecting (a) and (c) show that the $\omega_{RBM}$ of the prominent tube diameters observed in the $C_{60}$-DWNT bundles coincide with the $\omega_{RBM}$ of the inner and outer tubes of the isolated $C_{60}$-DWNTs [290].

to 13% in the wall to wall distance for this set of 11 DWNTs (all of which have (6,5) inner tubes) [290]. In such studies, the tube diameters $d_t$ and wall to wall distances between inner and outer tubes $\Delta d_{t,io}$ were determined from the radial breathing mode frequency-based on the relation between $\omega_{RBM}$ and $d_t$ developed for SWNTs (see Section 9.1.2). These estimates for $d_t$ should be considered as nominal values for $d_t$, and further work is needed to develop a corresponding relation between $\omega_{RBM}$ and $1/d_t$ that is valid for DWNTs. Because of the differences in the Coulomb interaction expected for the 4 different DWNT configurations, i. e., S@M, M@S, S@S and M@M, it is expected that even if a linear relation between $\omega_{RBM}$ and $1/d_t$ is retained for the inner and outer tubes of each DWNT configuration, the detailed relation will depend on the metallicity configuration of a given DWNT, as given above.

In the case of MWNTs, most of the samples are composed of tubes with diameters too large to exhibit observable RBM features. Although, in a few cases the

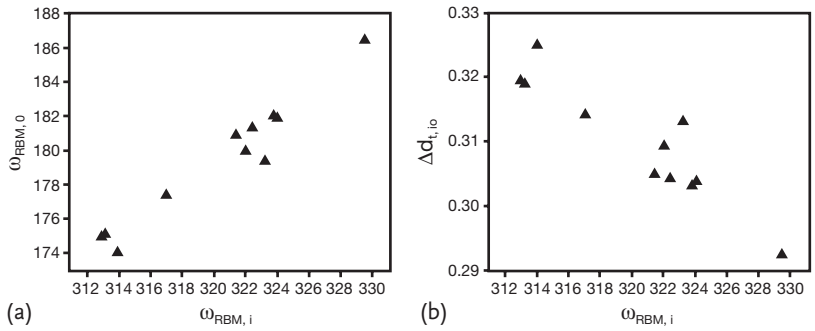


**Figure 9.6** All the inner tubes for the 11 peapod-DWNTs in this figure are (6,5) semiconducting tubes. (a) Plot of the $\omega_{RBM,i}$ of the inner tube vs. $\omega_{RBM,o}$ for the outer tubes which pair to form eleven different isolated DWNTs. (b) Plot of the nominal wall to wall distance $\Delta d_{t,io}$ for each of the 11 isolated DWNTs vs. $\omega_{RBM,i}$ shown in (a). An increase in the $\omega_{RBM,i}$ of the inner tubes (all are (6,5) tubes) is accompanied by a decrease in the measured nominal wall to wall $d_{t,io}$ distance [290].

inner tubes have small enough diameters ($d_t \lesssim 2\,nm$) and their RBM contributions can be seen [297], generally the RBM is not a reliable probe for studying and characterizing MWNTs.

### 9.1.4 Linewidths

The Raman spectral width is given by the lifetime of phonons. Several mechanisms can be responsible for the linewidth broadening of the resonance Raman features in SWNT spectra, including temperature-dependent effects (anharmonic processes, phonon–phonon and electron–phonon interactions and other effects), tube–tube/tube–substrate interactions, and nanotube defects (vacancies, substitutional and interstitial impurities, 7-5 structural defects, etc.), finite size effects, trigonal warping, as well as the energy separations between the incident or scattered photon and the pertinent van Hove singularity. Linewidth studies are best carried out at the single nanotube level where inhomogeneous broadening effects are minimized and linewidths approaching the natural linewidths for the various processes should be achievable.

Figure 9.7 shows the dependence of the RBM linewidth ($\Gamma_{RBM}$) on diameter $d_t$ for 170 SWNTs grown by CVD on a $Si/SiO_2$ substrate. It is noteworthy that $\Gamma_{RBM}$ values down to $4\,cm^{-1}$ are observed in individual SWNTs, since Raman peaks in $sp^2$ carbons are usually broader [242]. The low $\Gamma_{RBM}$ values are characteristic of 1D SWNTs. From the 170 data points in Figure 9.7, we clearly observe an increase in the average $\Gamma_{RBM}$ value (and also in the minimum value) with increasing $d_t$, that is, with increasing number of atoms along the circumference of the SWNTs. While this result might have a relation to intrinsic confinement effects related to the increase of the tube diameter, a tube flattening due to tube-substrate interaction

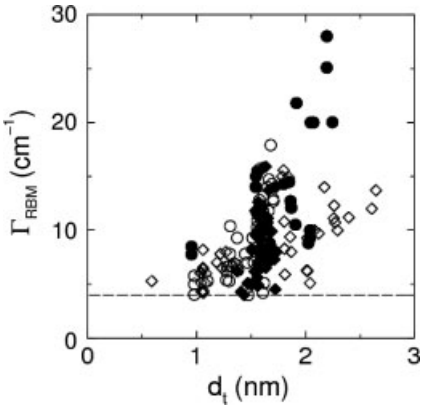


**Figure 9.7** $\Gamma_{\mathrm{RBM}}$ vs. $d_t$ for 81 M-SWNTs (filled symbols) and 89 S-SWNTs (open symbols) at 300 K. Circles indicate data obtained with the 2.41 or 2.54 eV laser excitation lines, and diamonds when obtained with a 1.58 eV laser [242].

is also expected to increase with increasing tube diameter, and this flattening may also play an important role in the observed linewidth dependence [298]. In the Raman spectra of SWNTs deposited in $Si/SiO_2$ substrates, RBM features are not often observed below $90\,\mathrm{cm}^{-1}$, although SWNTs with $d_t > 2.5\,\mathrm{nm}$ are not rare in this type of sample. The limited accuracy in identifying larger diameter tubes is probably caused by too large a broadening of the RBM peak.

### 9.1.5
### Beyond Elasticity Theory: Chiral Angle Dependence

There are two effects that are not considered by elasticity theory. The first is related to the chirality-dependent distortion of the lattice. The second is related to electron–phonon coupling in metallic SWNTs and is associated with the Kohn anomaly (see Section 8.4). These two effects can generate a chiral angle dependence of the RBM frequencies. The first effect should be observable in measurements made on small diameter ($d_t \sim 1\,\mathrm{nm}$) SWNTs, where the curvature-induced lattice distortion is important. The second is observed only in metallic SWNTs.

Results of $\omega_{\mathrm{RBM}}$ vs. $(d_t, \theta)$ (i. e., $(n, m)$) were obtained from SWNTs grown by the HiPCO (high pressure CO CVD) method and dispersed in surfactant aqueous solution [299]. The best linear relation fitting the RBM frequency dependence on diameter obtained for this sample was $\omega_{\mathrm{RBM}} = 218.3/d_t + 15.9$ (for a discussion of changes to the $\omega_{\mathrm{RBM}}$ vs. $d_t$ relation see Section 9.1.2). Figure 9.8 shows a plot of the deviations of $\omega_{\mathrm{RBM}}$ values from the best linear $1/d_t$ dependence that fits all the experimental data ($\Delta\omega_{\mathrm{RBM}} = \omega_{\mathrm{RBM}} - (218.3/d_t + 15.9)$) as a function of the chiral angle $\theta$. In this figure, one clearly sees deviations of the points from $\Delta\omega_{\mathrm{RBM}} = 0$, and these deviations are as large as $\Delta\omega_{\mathrm{RBM}} \sim \pm 3\,\mathrm{cm}^{-1}$, which is much larger than the experimental accuracy ($\simeq 1.0\,\mathrm{cm}^{-1}$).

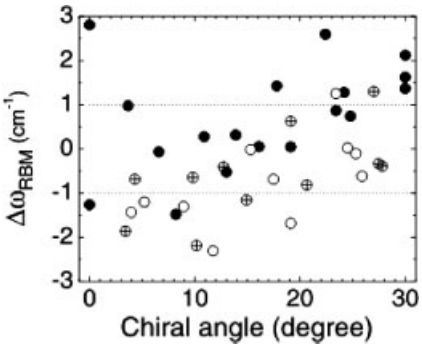


**Figure 9.8** Deviation of the experimentally observed RBM frequency ($\omega_{\mathrm{RBM}}$) from the linear dependence given by ($218.3/d_t + 15.9$), as a function of $\theta$ for a particular HiPCO nanotube sample [299]. Filled, open and crossed circles denote M-SWNTs, type I and type II S-SWNTs, respectively. The dotted lines show an experimental accuracy of $\pm 1\,\mathrm{cm}^{-1}$ [299].

Interesting trends can be seen from the deviations in Figure 9.8. The first is the observation of a systematically larger $\Delta\omega_{\mathrm{RBM}}$ for M-SWNTs (metallic SWNTs, solid bullets) when compared with S-SWNTs (semiconducting SWNTs, open bullets). The second is a $\Delta\omega_{\mathrm{RBM}}$ dependence on the chiral angle $\theta$, showing a clear increase in $\Delta\omega_{\mathrm{RBM}}$ with increasing $\theta$ from 0° (zigzag) to 30° (armchair), and both of these effects are stronger for metallic tubes.

Some of these deviations in $\omega_{\mathrm{RBM}}$ are due to curvature effects. For small $d_t$ SWNTs, curvature weakens the $sp^2$ chemical bonds which now have components along the circumferential direction, because of $sp^2$–$sp^3$ mixing. As a result, the RBM frequencies decrease with respect to their ideal values as the SWNT diameter decreases. Moreover, curvature destroys the isotropy of the elastic constants in SWNTs and therefore introduces a chirality dependence into $\omega_{\mathrm{RBM}}$. All these effects are well documented from a theoretical point of view [182, 300] where, by allowing the atoms to assume relaxed equilibrium positions for each $(d_t, \theta)$, the effective diameter changes could be determined. Kürti *et al.* [300] describe in detail the curvature effects on many structural properties of SWNTs. For instance, it is predicted that diameter deviations from the ideal $d_t$ values are roughly the same for zigzag and armchair tubes, but the changes in bond lengths are larger for the two C–C bonds with components along the circumferential direction for zigzag tubes as compared to the three such bonds for armchair tubes with similar diameter. This is a purely geometric effect, related to the directions of the three C–C bonds with respect to the circumferential direction. Therefore, in armchair tubes, the circumferential strain is more evenly distributed between the bonds, leading to smaller bond elongation. Since the RBM softening is directly related to the elongation of bonds along the circumference, a larger softening of $\omega_{\mathrm{RBM}}$ for zigzag tubes relative to armchair tubes is expected.

Finally, similar to the effect discussed for the G-band in Chapter 8, a phonon frequency shift of the radial breathing mode for M-SWNTs is predicted [275] and observed [301] as a function of Fermi energy, although a much smaller shift

($\sim 3\,\mathrm{cm}^{-1}$) due to the Kohn anomaly effect is expected for $\omega_{\mathrm{RBM}}$ than for $\omega_{\mathrm{G}}$. Armchair nanotubes will not show any renormalization-induced frequency shift while zigzag nanotubes will exhibit the maximum phonon softening. This chirality dependence originates from the $k$-dependent electron–phonon coupling for RBM phonons [275]. In the chiral and zigzag metallic SWNTs, a small energy gap is opened by the curvature of the cylindrical surface. When the curvature-induced gap is larger than $\hbar\omega_{\mathrm{RBM}}$, then the Kohn anomaly effect disappears. Since the gap is proportional to $1/d_{\mathrm{t}}^2$ and $\hbar\omega_{\mathrm{RBM}}$ is proportional to $1/d_{\mathrm{t}}$, there is a lower limit of $d_{\mathrm{t}}$ (1 to 1.8 nm depending on chiral angle) below which we cannot see the Kohn anomaly effect for the RBM phonon [275] .

## 9.2
## Intensity and the Resonance Raman Effect: Isolated SWNTs

The Raman effect as shown in Figures 9.1 and 9.9 for the RBM features is a resonant process. With the physics of $\omega_{\mathrm{RBM}}$ and $\Gamma_{\mathrm{RBM}}$ in place, next we consider the evolution of the RBM intensity as the laser excitation energy is varied. The range of laser energies over which the resonance Raman spectra is observed is called the resonance window (see Section 4.3.2).

### 9.2.1
### The Resonance Window

Strong resonant effects occur in the Raman scattering from an isolated SWNT when the energy of the incident or scattered light matches an optical transition $E_{ii}$ (see Section 2.3.4), thereby strongly enhancing the Raman signal [112, 136, 171, 176, 282, 303]. Therefore, it is possible to use the resonance Raman effect to study the electronic structure of individual SWNTs, and much effort has therefore been given to measuring the Raman spectra under resonant conditions [176, 302, 304–306]. In this section we review observations of the resonance window for the RBM feature.

Figure 9.9a shows an AFM image of a Si substrate with a thin $SiO_2$ surface coating [176, 307] and with lithographic markers on an $8 \times 8\,\mu\mathrm{m}^2$ lattice. Isolated SWNTs were grown on top of the substrate by a CVD method (see lines in Figure 9.9b). The light spot ($\sim 1\,\mu$m diameter) is positioned to be close to a mark ($\sim 1\,\mu$m size) (see Figure 9.9a) in order to achieve good precision in always returning the light spot to the same position on the sample as $E_{\mathrm{laser}}$ is changed. The dashed circles in Figure 9.9a,b display the position where the laser spot is placed, showing the presence of some isolated SWNTs. From the AFM measured SWNT heights, the diameters ($d_{\mathrm{t}}$) of the 11 SWNTs that lie within the light spot are determined, with $d_{\mathrm{t}}$ ranging from 0.7 nm to 1.9 nm (the AFM precision is about $\pm 0.2$ nm). Raman spectra of the sample were measured in the laser excitation wavelength (energy) range 720 nm (1.722 eV) $\leq E_{\mathrm{laser}} \leq$ 785 nm (1.585 eV) with steps of 4 nm ($\sim$ 0.009 eV), as shown in Figure 9.9c,d. All the anti-Stokes

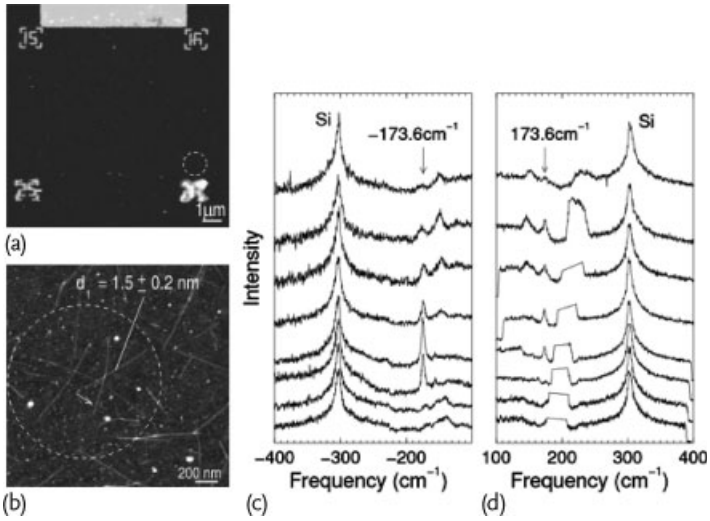


**Figure 9.9** (a,b) AFM image of the SWNT sample. Part (a) shows the markers used to localize the spot position (dashed circle) on the substrate during the Raman experiment and for further AFM characterization of the SWNTs that are located within the light spot indicated by the dashed circle in (b). (c) anti-Stokes and (d) Stokes Raman spectra from isolated SWNTs on a $Si/SiO_2$ substrate for several different laser excitation energies. From bottom to top, the spectra were taken at $E_{laser} = 1.623$, 1.631, 1.640, 1.649, 1.666, 1.685, 1.703, and 1.722 eV. The excitation was provided by a tunable Ti:Sapphire laser ($P < 10$ mW on the sample) pumped by an Ar ion laser (6 W). The incident light was filtered with a single-monochromator (Macpherson 1200 g/mm), and the scattered light was analyzed with an XY DILOR triple-monochromator, equipped with a $N_2$ cooled CCD detector. The Stokes signal quality (d) is not as good as that for the anti-Stokes signal (c) due to the frequency-dependent spectrometer efficiency that drops off rapidly with increasing laser wavelength, being worse in the Stokes frequency region. The flat region appearing in all the Stokes spectra in (d) comes from light leakage, and was cut out from the spectra [302].

(Figure 9.9c) and Stokes (Figure 9.9d) spectra were corrected to account for spectrometer efficiency at each laser energy, and the spectra were then normalized by the 303 $cm^{-1}$ Si substrate peak intensities. The anti-Stokes intensities were multiplied by $[n(\omega)+1]/n(\omega)$, where $n(\omega) = 1/[\exp(\hbar\omega/k_B T) - 1]$ is the Bose–Einstein thermal factor, $\omega$ is the RBM frequency, $k_B$ is the Boltzmann constant, and $T$ is the temperature (see Section 4.3.2.1). Although high laser power was used to measure the Raman spectra, $T$ was found to be close to room temperature (not higher than 325 K), and this was confirmed by changing the laser power from 1 $mW/\mu m^2$ (10 $MW/cm^2$) to 10 $mW/\mu m^2$ (100 $MW/cm^2$), where the Stokes/anti-Stokes intensity ratio for the 521 $cm^{-1}$ and nonresonant 303 $cm^{-1}$ Si peaks remained constant. Furthermore, the $\omega_{RBM}$ peak did not show a temperature-dependent shift, and the intensity ratios between the RBM features and the 303 $cm^{-1}$ Si peaks also remained constant in both the Stokes and anti-Stokes spectra [302].

With the light spot position shown in Figure 9.9a, the Raman spectra were measured with many different laser excitation energies. Figure 9.9 shows the anti-Stokes (c) and Stokes (d) Raman spectra of one light spot for several different laser excitation energies $E_{\text{laser}}$, increasing from the bottom to the top spectra (see caption). In Figure 9.9c,d, we see the RBM feature at 173.6 $\text{cm}^{-1}$ appearing and disappearing over the tunable energy range of $E_{\text{laser}}$, thereby allowing us to tune over the whole resonant window of one optical transition energy ($E_{ii}$) for this resonant SWNT. The linewidth for this $\omega_{\text{RBM}} = 173.6\,\text{cm}^{-1}$ peak is $\Gamma_{\text{RBM}} = 5\,\text{cm}^{-1}$, typical of that for one isolated SWNT (see Section 9.1.4) [176, 242]. The data points in Figure 9.10 show the peak intensity of the 173.6 $\text{cm}^{-1}$ RBM feature vs. $E_{\text{laser}}$ in the anti-Stokes (a) and Stokes (b) processes, which define the resonance window width $\Gamma$ for both the anti-Stokes and Stokes processes for the SWNT measured in Figure 9.9.

The RBM peak intensity $I(E_{\text{laser}})$, which is a function of $E_{\text{laser}}$, can be evaluated from Eq. (5.20) (Chapter 5). The first and second factors in the denominator of Eq. (5.20), respectively, describe the resonance effect with the incident and scattered light. Here $+(-)$ applies to the anti-Stokes (Stokes) process for the phonon of energy $E_{\text{ph}}$, while $\gamma_{\text{RBM}}$ gives the inverse lifetime for the resonant scattering pro-

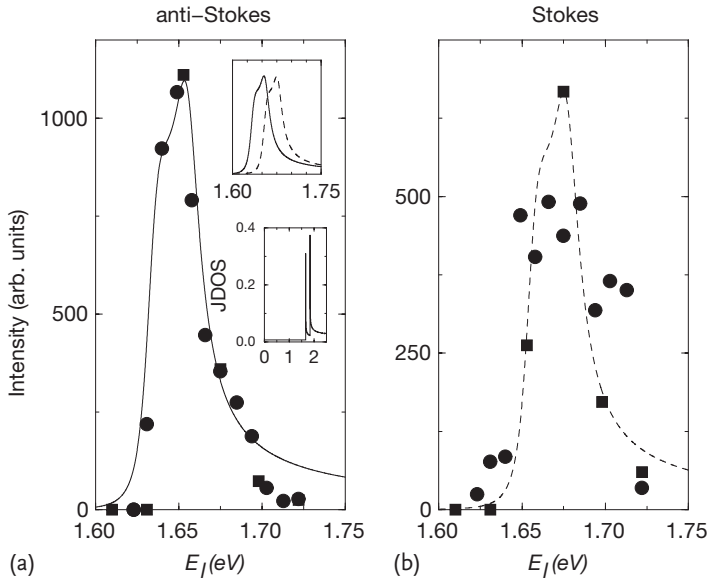


**Figure 9.10** Raman intensity vs. laser excitation energy $E_l$ for the $\omega_{\text{RBM}} = 173.6\,\text{cm}^{-1}$ peak (see Figure 9.9) for the (a) Stokes and (b) anti-Stokes Raman processes. Circles and squares indicate two different $E_{\text{laser}}$ runs on the same SWNT sample. The line curves indicate the resonant Raman window predicted from Eq. (5.20), with $E_{ii} = 1.655\,\text{eV}$, $\gamma_r = 8\,\text{meV}$, but taking the sum over internal states ($\sum_{m,m'}$) outside the square modulus. The upper inset compares the theoretically predicted Stokes and anti-Stokes resonant windows on an energy scale in eV, and the lower insert shows the joint density of states (JDOS) vs. $E_{\text{laser}}$ for this SWNT [302].

cess [308]. For simplicity, the matrix elements $M^d M^{ep} M^d$ can be considered to be independent of energy in this small energy range. Here $M^d$ and $M^{ep}$ are, respectively, the matrix elements for the electron-radiation (absorption and emission) and the electron–phonon interactions. Chapter 11 develops the theory for these matrix elements in detail.

The curves in Figure 9.10 show theoretical fits to the experimental data points for the Stokes (dashed line) and anti-Stokes (solid line) resonant windows for an (18,0) metallic zigzag SWNT, using $E_{ph} = 21.5$ meV obtained from $\omega_{RBM} = 173.6\,cm^{-1}$ [302]. Notice the asymmetric lineshape in the resonance windows. These fits were actually obtained in [302] by considering not a coherent Raman scattering process, but an incoherent scattering process, where the sum over the internal states ($\sum_{m,m'}$ in Eq. (5.20)) was taken outside the square modulus. However, this procedure is controversial, since this asymmetry could be generated by other resonance levels lying close in energy.

Disregarding the asymmetry aspect, the width of the resonant windows gives $\gamma_{RBM} = 8$ meV, in good agreement with previous measurements [171, 172, 309] and a transition energy of $E_{ii} = 1.655 \pm 0.003$ eV is also found. The upper inset to Figure 9.10 shows a comparison between the theoretically predicted Stokes and anti-Stokes resonant windows, revealing a shift in these resonant windows due to the resonant condition for the scattered photon, $E_s = E_{ii} \pm E_{ph}$ for the anti-Stokes (+) and the Stokes (−) processes, respectively. Therefore, by using a tunable laser, it is possible to study the resonance window for *one* isolated SWNT, giving its $E_{ii}$ value with a precision better than 5 meV at room temperature. Resonance windows for the RBM mode are, in fact, found to have a dependence on both diameter and chiral angle, as discussed in Section 9.3.2.

### 9.2.2
### Stokes and Anti-Stokes Spectra with One Laser Line

In the nonresonant Raman spectra, the anti-Stokes intensity is always smaller than the Stokes intensity, and the $I_{aS}/I_S$ intensity ratio can be used to measure the sample temperature (see Section 4.3.2.1). However, under sharp resonance conditions the $I_{aS}/I_S$ ratio strongly depends on the difference between the laser excitation energy $E_{laser}$ and the resonance energy $E_{ii}$. The $I_{aS}/I_S$ intensity ratio for the RBM then depends sensitively on $E_{ii} - E_{laser}$, and the $I_{aS}/I_S$ ratio for the RBM feature at $E_{laser}$ can be used to determine $E_{ii}$ experimentally to within 10 meV and to determine whether the resonance is with the *incident* or *scattered* photon [310].

Figure 9.11 shows both Stokes and anti-Stokes spectra for the RBM for another isolated SWNT sitting on a $Si/SiO_2$ substrate, which is similar to the SWNTs shown in Figure 9.9. The measured anti-Stokes intensity is already corrected by the Bose–Einstein thermal factor, and a temperature $T = 300$ K was found from the two Si phonon features also present in these spectra. In Figure 9.11a,b the normalized anti-Stokes intensity at $\omega_{RBM} = 253\,cm^{-1}$ is much larger than the Stokes intensity. This asymmetry in intensity between the anti-Stokes and Stokes RBM spectra can be quantitatively analyzed by using resonance Raman theory, and the resulting

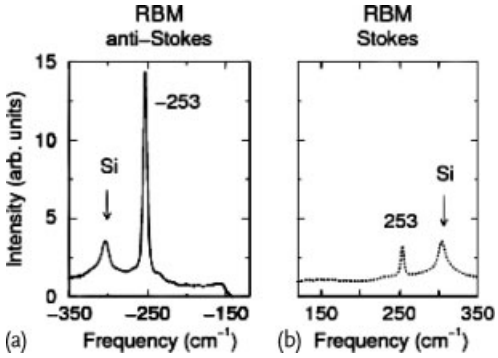


**Figure 9.11** (a) Resonant anti-Stokes and (b) Stokes Raman spectra of a (12,1) SWNT (as identified in [310]) on a $Si/SiO_2$ substrate, using $E_{laser} = 1.579\,eV$ (758 nm). The peak at $\pm 303\,cm^{-1}$ comes from the Si substrate. The RBM frequencies are displayed in $cm^{-1}$.

resonance window $I(E_{laser})$ for both the anti-Stokes and Stokes spectra from one isolated tube can be calculated using Eq. (5.20).

### 9.2.3
### Dependence on Light Polarization

As discussed in Chapter 6, the totally symmetric Raman-active modes ($A_1$ symmetry) can only be observed when both the incident and scattered light are polarized along the tube ($ZZ$), or perpendicular to the tube axis ($XX$). In the ($ZZ$) scattering configuration, an optical transition is allowed between electronic states with the same angular momenta, that is, $E_{\mu\mu} = \mathbb{E}_{\mu}^{(v)} \rightarrow \mathbb{E}_{\mu}^{(c)}$ (see Section 6.4.5). Such a transition is equivalent to the usual $E_{ii}$ transitions denoted in the Kataura plot (see Section 2.3.4). In the ($XX$) scattering configuration, an optical transition is allowed between electronic states with different angular momenta, that is, $E_{\mu\mu} = \mathbb{E}_{\mu}^{(v)} \rightarrow \mathbb{E}_{\mu\pm1}^{(c)}$. Such transitions are usually denoted by $E_{i,i\pm1}$, and they differ in energy from the usual transition energies $E_{ii}$ [311]. There have been strong efforts to characterize such transitions, using polarized photoluminescence spectra [40, 312].

Since the RBM features from isolated SWNTs are seen only under resonance conditions, it is expected that the RBM from a single carbon nanotube will be seen in the ($ZZ$) and ($XX$) polarizations for different laser excitation energies. The polarization dependence of the Raman intensity related to the laser excitation energy has been called the *antenna* effect. This antenna effect was first reported by Duesberg *et al.* [235] (see Figure 9.12) and later by others [226–228, 313–315].

In general the intensity of the ($XX$) polarized spectra should be strongly suppressed by the so-called *depolarization* effect. Ajiki and Ando [238] have calculated the optical conductivity of carbon nanotubes taking into account this depolarization effect, and they found that the absorption of light polarized parallel to the tube axis ($Z$) is up to 20 times larger than that for perpendicularly polarized light ($X$).

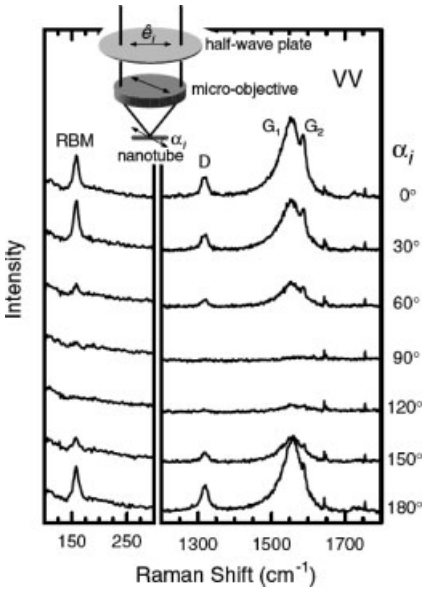


**Figure 9.12** Raman spectra of an isolated SWNT (or a thin rope of SWNTs) in the $VV$ configuration for various angles $\alpha_i$ between the tube axis and the polarization of the incident laser beam, as depicted in the inset. For $\alpha_i = 0°$ and $180°$ ($VV = ZZ$), the polarization of the incident radiation is parallel to the axis of the SWNTs determined from scanning force microscopy images with an accuracy of $\pm 10°$ [235].

This leads to a strongly reduced Raman signal when the polarization of the incident radiation is perpendicular to the nanotube axis. This polarization behavior has been demonstrated experimentally in SWNT bundles, where many $(n, m)$ tubes are present and both $E_{ii}$ and $E_{i,i\pm1}$ can be determined for specific tubes using the same sample with the same excitation laser energy [316].

## 9.3 Intensity and the Resonance Raman Effect: SWNT Bundles

In this section the resonance window analysis introduced in the previous section will be extended to SWNT ensembles. Through the RBM resonance window analysis, we can study the $(n, m)$ dependence of the optical transition energies ($E_{ii}$). This analysis reveals a great deal of information that goes beyond the simple tight-binding method described in Chapter 2, including $\sigma-\pi$ hybridization and utilizing the science of excitons. The optical transition energies in SWNTs which are sensitive to these excitonic effects have been studied in detail through fluorescence and Raman spectroscopy experiments [80, 183, 185]. Though some aspects of the experiments can be interpreted within the context of a simple, noninteracting electron model [182, 299], it has become increasingly clear that electron–electron interac-

tions also play an important role in determining the optical transition energies. Finally, SWNTs represent one of the best known materials system for the study of exciton photophysics, both from a theoretical and experimental viewpoint. Since SWNTs involve only carbon atoms, theoretical calculations can be carried out by using a relatively simple model Hamiltonian, as discussed in Chapter 10.

### 9.3.1
### The Spectral Fitting Procedure for an Ensemble of Large Diameter Tubes

In isolated SWNTs (Section 9.2.1), or even in ensembles of small $d_t$ SWNTs (briefly discussed in Section 4.4.2, see Figure 4.13a), each radial breathing mode (RBM) in resonance with a given excitation laser line ($E_{laser}$) is spectrally well-defined in frequency ($\omega_{RBM}$), so that the RBM peaks and resonance profiles can be clearly identified. When larger $d_t$ SWNTs are present and the differences in $\omega_{RBM}$ become smaller than the RBM linewidth, the RBM peaks cannot be clearly resolved and the spectra exhibit broad RBM features with contributions from several different $(n, m)$ SWNTs. Therefore, fitting the Raman spectra becomes complex. It is then necessary to establish a systematic procedure to perform the Raman spectral analysis.

Figure 9.13a shows the RBM Raman spectrum obtained from the "alcohol-assisted" SWNTs using $E_{laser} = 1.925$ eV (644 nm) [287]. The bullets show the data points and the solid line shows the fit obtained using 34 Lorentzian curves (the peaks below the spectral curve in Figure 9.13a). Each Lorentzian curve can be related to the RBM from SWNTs with the same $(n, m)$ index. The dark gray Lorentzians represent the RBM from M-SWNTs and the light gray Lorentzians represent the RBM from S-SWNTs. To determine how many Lorentzians should be used to fit

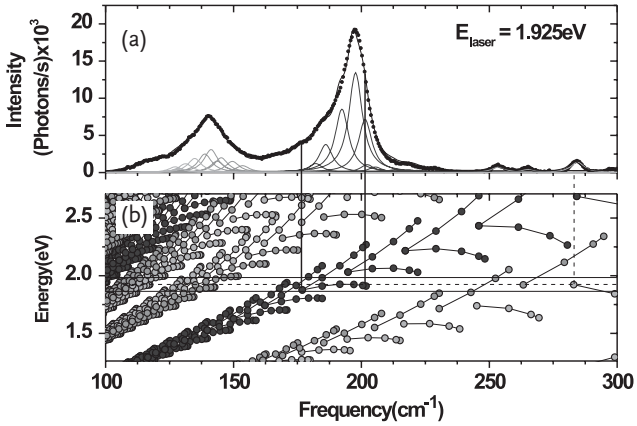


**Figure 9.13** (a) Raman spectrum (bullets) obtained with a 644 nm laser line ($E_{laser} = 1.925$ eV). This spectrum was fitted by using 34 Lorentzians (curves under the spectra) and the solid line is the fitting result. (b) The Kataura plot used as a guide for the fitting procedure (from EPAPS material in [287]).

each resonance spectrum, we use the Kataura plot (see Figure 9.13b). The dashed horizontal line in Figure 9.13b represents the excitation energy for the spectrum shown in Figure 9.13a, and the two bold horizontal lines (above and below the dashed line) give the approximate boundary for the RBM resonance profiles (see detailed discussion in Section 9.3.2). To fit the spectrum shown in Figure 9.13a we expect that transitions corresponding to all the bullets inside the rectangle limited by the two bold lines should occur. The vertical bold lines connecting Figure 9.13a,b indicate that the metallic $2n + m = 30$ family is in resonance with the laser excitation energy 1.925 eV, while the dashed vertical line shows the RBM feature from the (7, 5) SWNT.

The difficulty in performing the spectral fitting is due to the large number of Lorentzian curves needed to fit a broad RBM profile [282]. The fitting program tends to broaden and increase some peaks, while eliminating others. If for the same fit one Lorentzian is shifted by a couple of $\mathrm{cm}^{-1}$, the fitting program will return a completely different fitting result. Therefore, some constraints for the peak frequencies and spectral linewidths (full width at half maximum (FWHM)) must be applied. For example, the $\omega_{\mathrm{RBM}}$ obey the relation $\omega_{\mathrm{RBM}} = (227/d_{\mathrm{t}})\sqrt{1 + C_e/d_{\mathrm{t}}^2}$, which correctly describes environmental effects by changing $C_e$ and this relation is discussed in detail in Section 9.1.2. For lack of information, we may have to require all the Lorentzian peaks in one experimental spectrum to share the same FWHM value.

After analyzing all the spectra such as shown in Figure 9.13a, the Raman intensity at each RBM frequency has to be plotted as a function of $E_{\mathrm{laser}}$. Such a plot gives the resonance profile for the $(n, m)$-specific SWNTs that have the specified RBM frequency. The RBM peak intensity $I(E_{\mathrm{laser}})$, which is a function of $E_{\mathrm{laser}}$, can be evaluated from Eq. (5.20) or, alternatively, by using a simplification of this equation given by

$$I(E_{\mathrm{laser}}) \propto \left| \frac{1}{(E_{\mathrm{laser}} - E_{ii} - i\gamma_{\mathrm{RBM}})(E_{\mathrm{laser}} - E_{ii} \pm E_{\mathrm{ph}} - i\gamma_{\mathrm{RBM}})} \right|^2 . \tag{9.9}$$

To illustrate the fitting procedure, Figure 9.14 shows three resonance profiles (black bullets), one in the near-infrared range (a), one in the visible range (b), and one in the near-ultraviolet range (c). The three resonance profiles were fitted according to resonance Raman scattering theory (solid line, from Eq. (9.9), and the values obtained for $E_{ii}$ are indicated in Figure 9.14 (as well as for $\omega_{\mathrm{RBM}}$ and $(n, m)$) [287, 317]. Notice the resonance window width for SWNTs in bundles (usually within 40–160 meV range) are much broader than for isolated SWNTs (see Figure 9.10).

### 9.3.2
### The Experimental Kataura Plot

In this section, the resonance window analysis is extended to all $(n, m)$ SWNTs, from where we can study the $E_{ii}$ dependence on $(d_{\mathrm{t}}, \theta)$. Figure 9.15a shows a 2D RBM map for the water-assisted CVD grown (here called the "super-growth", S.G. [281]). SWNT sample. This sample has a very broad diameter distribution, and

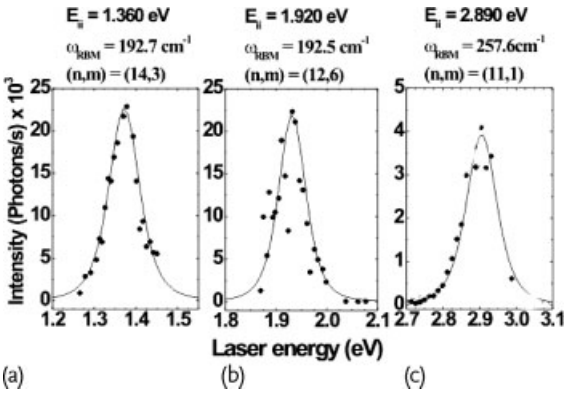


**Figure 9.14** Resonance windows for specific $(n, m)$ SWNTs within a bundle. (a) Resonance profile (black dots) in the near-infrared range for $\omega_{\mathrm{RBM}} = 192.7\,\mathrm{cm}^{-1}$. The data for tube (14,3) was fitted (solid line) using Eq. (9.9) with $\gamma_{\mathrm{RBM}} = 0.065\,\mathrm{eV}$ and $E_{ii} = 1.360\,\mathrm{eV}$. (b) Resonance profile in the visible range is shown for $\omega_{\mathrm{RBM}} = 192.5\,\mathrm{cm}^{-1}$ (tube (12,6)), with $\gamma_{\mathrm{RBM}} = 0.045\,\mathrm{eV}$ and $E_{ii} = 1.920\,\mathrm{eV}$. (c) Resonance profile in the near-ultraviolet range is shown for $\omega_{\mathrm{RBM}} = 257.6\,\mathrm{cm}^{-1}$ (tube (11,1)), with $\gamma_{\mathrm{RBM}} = 0.073\,\mathrm{eV}$ and $E_{ii} = 2.890\,\mathrm{eV}$ (from EPAPS material in [287]).

can be used to gain a deep understanding of the SWNT optical properties. For the construction of the experimental Kataura plot in Figure 9.15a, 125 different laser lines were used [189, 317]. By fitting each of the spectra with Lorentzians, $(n, m)$ indices were assigned to 197 different SWNTs.[4)]

Figure 9.15b is a plot of all $E_{ii}^{\mathrm{S.G.}}$ obtained experimentally by fitting the resonance windows extracted from the data in Figure 9.15b, as a function of $\omega_{\mathrm{RBM}}^{\mathrm{S.G.}}$. The observed $E_{ii}^{\mathrm{S.G.}}$ ranges from $E_{11}^{S}$ up to $E_{66}^{S}$ (the superscripts S stand for semiconducting S-SWNTs and M for metallic M-SWNTs). Finally, all the $E_{ii}^{\mathrm{S.G.}}$ data in Figure 9.15b can be fitted using an empirical equation that is discussed below and given by [282, 287, 318]:

$$E_{ii}(p, d_{\mathrm{t}}) = \alpha_p \frac{p}{d_{\mathrm{t}}} \left[ 1 + 0.467 \log \frac{0.812}{p/d_{\mathrm{t}}} \right] + \beta_p \cos 3\theta / d_{\mathrm{t}}^2 \,, \tag{9.10}$$

where $p$ is defined as $1, 2, 3, \ldots, 8$ for $E_{11}^{S}$, $E_{22}^{S}$, $E_{11}^{M}$, $E_{33}^{S}$, $E_{44}^{S}$, $E_{22}^{M}$, $E_{55}^{S}$, $E_{66}^{S}$, thus measuring the distance of each cutting line from the $K$ point in the zone-folding procedure. The fitting gave values $\alpha_p = 1.074$ for $p = 1, 2, 3$ and $\alpha_p = 1.133$ for $p \geq 4$. The $\beta_p$ values for the lower (upper) $E_{ii}$ branches are $-0.07(0.09)$, $-0.18(0.14)$, $-0.19(0.29)$, $-0.33(0.49)$, $-0.43(0.59)$, $-0.6(0.57)$, $-0.6(0.73)$ and $-0.65$ (unknown) for $p = 1, 2, 3, \ldots, 8$, respectively [317, 318]. The functional form in Eq. (9.10) carries a linear dependence of $E_{ii}$ on $p/d_{\mathrm{t}}$, as expected from the tight-binding theory plus quantum confinement of the 2D electronic structure of graphene, a logarithmic correction term that comes from many-body interactions, and a $\theta$-dependent term which includes electronic trigonal warping and chirality-dependent curvature

4) The data for Figure 9.2 came from this experiment [189, 317].

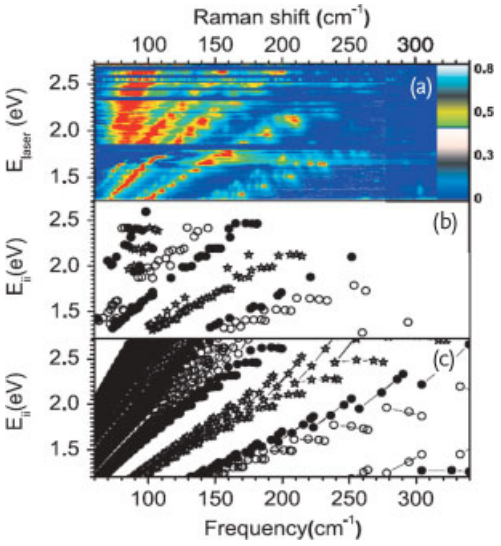


**Figure 9.15** (a) RBM resonance Raman map for the "super-growth" (S.G.) SWNT sample [189, 317, 318]. (b) Kataura plot of all transition energies ($E_{ii}^{S.G.}$) that could be experimentally obtained from the resonance windows extracted from (a), as function of $\omega_{RBM}$. (c) Kataura plot obtained from Eq. (9.10) with the parameters that best fit the data in (b). The stars stand for M-SWNTs, the open bullets stand for type I S-SWNTs and the filled bullets stand for type II S-SWNTs [317].

effects ($\sigma-\pi$ hybridization) [287]. The theoretical understanding of all these factors will be discussed in Chapter 10.

## 9.4 Summary

In this chapter we show how the RBM spectra from single-wall carbon nanotubes can be used to study the concepts of resonance Raman scattering in detail. Although resonance Raman scattering should be observable in every nanocarbon material, the RBM for carbon nanotubes is special because of the one-dimensional physics of carbon nanotubes and the low RBM energy. These two properties, together, generate a very sharp resonance window for RBMs. Furthermore, the RBM frequency depends on tube diameter, as explained here using elasticity theory. Due to this $d_t$ dependence, the RBM from different $(n, m)$ tubes can be identified, and used to study, through the resonance effect, the electronic structure of the carbon nanotubes, as well as environmental effects. This electronic structure is summarized in the empirical Eq. (9.10), which is related to many physical concepts that will be discussed in the next chapter.

**Problems**

[9-1] Obtain the density of graphite in kg/m$^3$. Here we can use the in-plane C–C distance which is 1.42 Å and the interlayer distance between two graphene layers which is 3.35 Å and note that about 2% of the carbon atoms in graphite are $^{13}$C and the remaining 98% are $^{12}$C. For this problem we need at least three digits in numerical accuracy.

[9-2] When the radius of a zigzag SWNT is modified by $\delta R$, determine by how much the C–C distance is modified along the circumferential direction.

[9-3] The Young's modulus of graphene is $Y = 1060$ GPa. Obtain the sound velocity of the LA phonon mode by calculating the nanotube density.

[9-4] The Young's modulus of SiC, Fe and diamond are, respectively, $Y = 450$, 200, 1200 GPa. Obtain sound velocities for these materials.

[9-5] Obtain the sound velocities for an ideal air sample in units of m/s and km/h.

[9-6] Obtain the formula for the sound velocity for the TA phonon mode $C_t = \sqrt{G/\rho}$, where G, the shear modulus, is given by $G = Y/(2(1+\nu))$, and where $Y$ and $\nu$ are the Young's modulus and Poisson ratio, respectively.

[9-7] Evaluate $A$ in Eq. (9.4) in cm$^{-1}$ units.

[9-8] Check that all terms in Eq. (9.5) are dimensionless.

[9-9] Obtain Eq. (9.6) from Eq. (9.5). Note that a factor $1/2\pi c$ appears when we measure $\omega$ in units of cm$^{-1}$. Using the known values for the various factors, get the value of 227 for $\omega_{\mathrm{RBM}}$ in units of cm$^{-1}$ for $d_{\mathrm{t}} = 1$ nm.

[9-10] Calculate the shift of $\omega_{\mathrm{RBM}}$ in Eq. (9.7) for $d_{\mathrm{t}} = 1$ nm and 2nm.

[9-11] Estimate $C_e$ in Eq. (9.8) and the diameter at which the correction term $C_e d_{\mathrm{t}}^2$ becomes 0.21.

[9-12] Explain that the anharmonic term in the vibrational Hamiltonian gives a finite lifetime to the phonon which is responsible for the Raman spectral width.

[9-13] Using the uncertainty relation between energy and time, obtain the phonon lifetime for Raman spectra with a spectral width of 1 cm$^{-1}$ and of 10 cm$^{-1}$.

[9-14] Evaluate the electric field in V/m for a laser power of 1 mW/$\mu$m$^2$.

[9-15] For $T = 300$ K and 77 K, what is the intensity ratio of the Stokes to anti-Stokes *nonresonant* Raman signals for a 173.6 cm$^{-1}$ RBM phonon? How about for a 1590 cm$^{-1}$ G-band?

[9-16] Measure the resonance window values from Figure 9.10 and estimate the lifetime of photoexcited carriers. Explain by giving some reasons for which

lifetime is shorter, the lifetime of the photoexcited carriers or the lifetime of phonons.

[9-17] For 785 nm laser light, obtain the wavelength in nm for the Stokes and anti-Stokes scattered light for a 173.6 $cm^{-1}$ RBM phonon.

[9-18] For 785 nm laser light, what is the $E_{ii}$ energy of the scattered light resonance conditions for the Stokes and anti-Stokes Raman spectra for a 173.6 $cm^{-1}$ RBM phonon?

[9-19] Give the expected intensity ratio $I_S/I_{aS}$ between the Stokes and anti-Stokes RBM signals shown in Figure 9.10 for $E_{\text{laser}} = 1.63$ eV, $E_{\text{laser}} = 1.65$ eV and $E_{\text{laser}} = 1.67$ eV. Consider both $T = 0$ K and $T = 300$ K.

[9-20] Explain why the intensity ratio of the Stokes to anti-Stokes resonance Raman intensity for one laser energy might not give the temperature of the sample. For the nonresonance Raman intensity, on the other hand, we may get the information needed to determine the temperature. Why?

[9-21] Consider that the spectra in Figure 9.11 were obtained from a SWNT with $\gamma_{\text{RBM}} = 8$ meV. Using Eq. (9.9), find the value of $E_{ii}$ which gives the observed $I_S/I_{aS}$.

[9-22] Build your own Kataura plot using Eq. (9.10). Evaluate the $E_{22}^S$ and $E_{33}^S$ energies for the (6,5), (11,1), (10,5) SWNTs by using Eq. (9.10).

[9-23] There are two definitions for the type of semiconducting SWNTs; one is Type I and Type II using (mod$(2n + m, 3) = 1$ and $= 2$), and the other is Mod 1 and 2 using mod$(n - m, 3) = 1, 2$. Show that Type I and Mod 2 (or Type II and Mod 1) are equivalent to each other.

[9-24] In the $(n, m)$ map of SWNTs, show that SWNTs with $2n + m =$ const. have a similar diameter while SWNTs with $n - m =$ const. have a similar chiral angle. Explain that the $2n + m =$ const. family is suitable for studying the chiral angle dependence while that $n - m =$ const. family is suitable for studying the diameter dependence.